

All-Optical Cochlear Implants

Stylianos E. Trevlakis¹, *Student Member, IEEE*,

Alexandros-Apostolos A. Boulogeorgos², *Senior Member, IEEE*,

Nestor D. Chatzidiamantis³, *Member, IEEE*, and George K. Karagiannidis⁴, *Fellow, IEEE*

Abstract—In the present work, we introduce a novel cochlear implant (CI) architecture, namely all-optical CI (AOCI), which directly converts acoustic to optical signals capable of stimulating the cochlear neurons. First, we describe the building-blocks (BBs) of the AOCI, and explain their functionalities as well as their interconnections. Next, we present a comprehensive system model that incorporates the technical characteristics and constraints of each BB, the transdermal-optical-channel particularities, i.e., optical path-loss and external-implanted device stochastic pointing-errors, and the cochlear neurons biological properties. Additionally, in order to prove the feasibility of the AOCI architecture, we conduct a link-budget analysis that outputs novel closed-form expressions for the instantaneous and average photon flux that is emitted on the cochlear neurons. Likewise, we define three new key-performance-indicators (KPIs), namely probability of hearing, probability of false-hearing, and probability of neural damage. The proposed theoretical framework is verified through respective simulations, which not only quantify the efficiency of the proposed architecture, but also reveal an equilibrium between the optical transmission power and the patient’s safety, as well as the AOCI BBs specifications. Finally, it is highlighted that the AOCI approach is greener and safer than the conventional CIs.

Index Terms—Average photon flux, biomedical communications, cochlear implants, feasibility study, link-budget, optogenetics, transdermal optical communications.

NOMENCLATURE

ABR	Auditory brainstem response
AOCI	All-optical cochlear implant
CCI	Conventional cochlear implant
CI	Cochlear implant
CL	Coupling lens
DSP	Digital signal processing
FBG	Fiber Bragg grating
GL	Guided lens

KPI	Key performance indicator
LD	Laser diode
LED	Light emitted diode
LS	Light source
MEM	Microelectromechanical
MPE	Maximum permissible exposure
OF	Optical fiber
PDF	Probability density function
PMF	Probability mass function
RF	Radio frequency
SNR	Signal-to-noise-ratio
TOL	Transdermal optical link.

I. INTRODUCTION

OVER half a million patients worldwide, suffering from mild-to-severe hearing loss, regain their speech perception with the aid of cochlear implants (CIs) [1]. Conventional CIs (CCIs) consist of an external device that converts the audio into radio frequency (RF) signals and emits them to an implanted device. The latter processes the received signals in order to convert them into electrical ones, which stimulate the acoustic nerve. The main bottlenecks of the CCIs are twofold: (i) The poor coding of spectral information due to the wide spread of electric current from each electrode, which results in broad excitation of the cochlear neurons; and (ii) The bandwidth scarcity on the RF spectrum that significantly constraints the achievable data rate; hence, the faithful reproduction of the neural stimulus [2]–[5].

A. State Of the Art and Motivation

In order to surpass the electrical stimulation constraints, a great amount of research effort has been directed toward alternative neural stimulation mechanics. One of the most promising concepts is the excitation of the neurons via optical signals [1], [6]–[10]. This approach is widely known as optogenetic stimulation and utilizes optical radiation in the wavelengths from 450 to 600 nm. Optogenetic interfaces are characterized by increased spatial resolution in comparison with electrical ones, and present higher tolerance for unwanted stimulation artifacts that interfere with the desirable stimulation [11]. Aspired by this, in [6], the authors experimentally verified that optogenetic cochlear stimulation achieves increased temporal fidelity with low-light intensities. This reveals that optogenetics can be used to develop CIs with improved restorative capabilities. Likewise, in [7]–[9], the narrow-light-spread in the cochlea was revealed, and it

Manuscript received February 4, 2020; revised April 11, 2020; accepted May 13, 2020. Date of publication May 22, 2020; date of current version July 15, 2020. The work of Stylianos E. Trevlakis was supported by the Hellenic Foundation for Research and Innovation (HFRI) under the HFRI Ph.D. Fellowship under Grant 480. The associate editor coordinating the review of this article and approving it for publication was J.-W. Choi. (Corresponding author: Alexandros-Apostolos A. Boulogeorgos.)

Stylianos E. Trevlakis, Nestor D. Chatzidiamantis, and George K. Karagiannidis are with the Department of Electrical and Computer Engineering, Aristotle University of Thessaloniki, 54124 Thessaloniki, Greece (e-mail: trevlakis@auth.gr; nestoras@auth.gr; geokarag@auth.gr).

Alexandros-Apostolos A. Boulogeorgos is with the Department of Electrical and Computer Engineering, Aristotle University of Thessaloniki, 54124 Thessaloniki, Greece, and also with the Department of Digital Systems, University of Piraeus, 18534 Piraeus, Greece (e-mail: al.boulogeorgos@ieee.org).

Digital Object Identifier 10.1109/TMBMC.2020.2996629

was indicated that excitation can be achieved with optogenetic stimulation with emitter intensities in the order of mW. Note that, the CCI requires transmission power of approximately 40 mW [3]. Specifically, as reported in [9], optically evoked auditory responses can be successfully measured with stimulations as low as 1 mW, while higher light-intensity will result in increased amplitude and decreased latency. In [7] and [9], it was proven that light in the range of 470 - 640 nm can be transmitted through optical fibers with diameter of some decades of μm and cause neural stimulation. Moreover, in [10], the authors explored the fundamental requirements for developing a light delivery system for the cochlea and provided practical implementations. Finally, in [1], the state-of-the-art on the emerging concept of optogenetic stimulation of the auditory pathway was presented, while the need for engineering novel multi-channel optical implants was highlighted.

In order to deal with the limitations of the RF band, the optical wireless CI (OWCI) architecture was introduced and studied in [12]. In the same contribution, the authors prove that OWCIs are capable of significantly improving the reliability, spectral and power efficiency by replacing the transdermal RF with an optical link. In addition, the OWCI can achieve capacity in the order of Mbps with only few μW , in contrast to the CCI, which requires at least few mW in order to achieve the same capacity. Finally, the utilization of the optical frequency band provides large amounts of unexploited, non-standardized, almost-interference-free bandwidth with increased safety for the human organism. This approach relied on several prior published works that had experimentally proven the feasibility of the transdermal optical link (TOL) [13]–[15]. In particular, in [13], TOLs were used to establish transdermal high-data-rate links. In [14], the key design parameters of transdermal OWC systems and their interactions were identified, accompanied by several design tradeoffs. In [15], Liu *et al.* evaluated the performance of TOLs utilized for clinical neural recording purposes in terms of data-rate and transmission power. In the same work, the characteristics of the receiver were investigated with regard to its size minimization and the signal-to-noise-ratio (SNR) maximization. Despite the excellency in transmission data-rate that OWCI provide, they cannot fully counterbalance the poor coding of spectral information in the acoustic nerve, since they carry the constraints of the electrical stimulation units. Likewise, their internal device has significant energy demands that arise from the existence of its energy-consuming digital signal processing (DSP) unit.

Based on the aforementioned research works and in combination with opto-electronic advances, several optical fiber (OF) designs were developed in order to output light in pre-determined locations along the fiber body [16]–[20]. In more detail, in [17], Nguyen *et al.* presented a multi-point, side-firing OF capable of emitting light at multiple locations with power up to 25% of the total coupled light. Furthermore, in [18], Pisanello *et al.* developed a single OF capable of delivering light to the target area through multiple target windows, while, in [19], [20], the influence of several design parameters (i.e., input angle of light, numerical aperture) on the OF output light were investigated. These OFs were

proposed for neural stimulation in several biomedical applications, including cochlear stimulation (see, e.g., [1] and references therein).

B. Contribution

To sum up, the hitherto proposed architectures either counterbalance the nerve stimulation limitation or the RF scarcity issue, but, none of them solves the combined problem. An architecture that would convert the audio into optical signal in the external device and transmit it directly to the cochlear nerve, would not only counterbalance the aforementioned challenges, but, it would also eliminate the necessity for an energy consuming implanted DSP device. Aspired by this, in this contribution, we propose an innovative architecture, termed as all-optical CI (AOCI), which not only exploits the characteristics of its predecessors but also is able to break their barriers. While the proposed architecture takes advantage of the beneficial particularities of the OWCI, it introduces significant modifications. The most important one is that, the AOCI is comprised only by passive components. As a result, the internal device has no power demands, thus, the proposed system is characterized by higher energy efficiency and eliminates the need of designing sophisticated power transfer approaches. Additionally, the utilization of light for the excitation of the neuron of the cochlea provides higher fidelity compared to electrical stimulations, due to the fact that light is characterized by lower spread through the human tissue. In more detail, the contribution is outlined below:

- We introduce the AOCI architecture and explain its building blocks (BBs) as well as their usage and functionalities.
- We present a novel system model that accommodates the particularities of each BB, such as the light source (LS) divergence angle, the dimensions of the optical components, the channel characteristics, such as its path-gain, and the pointing errors, as well as the biological peculiarities of the human body, like the existence of neural noise.
- We study the AOCI feasibility and efficiency by providing the theoretical framework that quantifies its performance in terms of the average stimulation photon flux, with regard to the LS emitted optical power as well as each BBs specifications.
- Finally, a side, yet important, contribution of this work is that we extract a novel closed-form expression for the instantaneous coupling efficiency in the presence of stochastic pointing errors.

C. Structure

The remainder of this paper is organized as follows: Section II presents the architecture of the AOCI, followed by the system model of the AOCI that is described in Section III. In Section IV, we provide the analytic framework for accessing the feasibility and efficiency of the AOCI. Respective numerical and simulation results, which illustrate the performance of the AOCI and validate the theoretical framework, alongside useful related discussions are provided in Section V. Finally,

closing remarks and a summary of the main findings of this contribution are presented in Section VI.

D. Notations

Unless stated otherwise, $|\cdot|$ denotes absolute value, $\exp(\cdot)$ represents the exponential function, while $\log_{10}(\cdot)$ stands for the decadic logarithm. In addition, $P_r(\mathcal{A})$ denotes the probability of the event \mathcal{A} , whereas $\text{erf}(\cdot)$ denotes the error function. Also, $J_\nu(\cdot)$ represents the Bessel function of the first kind and the ν -th order, while $I_\nu(\cdot)$ represents the modified Bessel function of the first kind and the ν -th order. Finally, $\Gamma(\cdot)$ is the Gamma function and $\Psi_2(\cdot)$ represents the fifth Humbert hypergeometric series [21, eq. (7.2.4/10)]. Finally, $F^{(4)}\left[\begin{matrix} \cdot \\ \cdot \end{matrix}; \cdot, \cdot, \cdot, \cdot\right]$ is the generalized quadruple hypergeometric function [22, eq. (16)].

II. THE AOCI ARCHITECTURE

As illustrated in Fig. 1, the AOCI architecture consists of two devices; the external and the implanted. Much like the conventional cochlear implant, the external device is fixed on the outer surface of the skin, while the implanted one is attached on the bone of the skull, right under the skin. As a result, the total distance of the communication link is the skin thickness, which is proven to be in the range of 2-4 mm for the area of the skull [23]. However, in our analysis we have considered a more pessimistic approach by considering skin thickness values between 4 and 10 mm. The role of the external device is to capture the acoustic signal with a microphone, perform the necessary digital signal processing and convert it into an optical one, which is suitable for the stimulation of the acoustic nerve. Afterwards, it transmits the optical signal to the implanted device. Notice that, the main difference of the external unit of the AOCI with the corresponding CCI is that the RF front-end is replaced with a LS connected to its driver. This LS can be a light emitting diode (LED) or a laser diode (LD). The implanted unit consists of a guiding lens (GL), a microelectromechanical (MEM) device, a coupling lens (CL) and an OF. The GL is used in order to maximize the optical power captured by the implanted device via guiding the light toward the MEM, which in turn couples it into the OF via the CL. Finally, the coupled light propagates through the OF and is emitted on the photosensitive neurons of the cochlea. Next, we present in more detail the functionalities of the main BBs of the implanted device.

MEM: Due to the unique nature of each human body (i.e., different skin thickness and color, etc.), the need arises of designing a flexible externally-operated light direction controlling system that is able to adjust AOCI to the human bodies particularities. Any failure to align the optical beam properly will result to loss of communication and, therefore, hearing loss. The solution is provided through the utilization of the MEM system, which have been greatly analyzed over the past couple of decades, due to its reduced size, light-weight and low-cost [24]–[26]. This system can be configured in order to not only mitigate any imperfections during the implantation

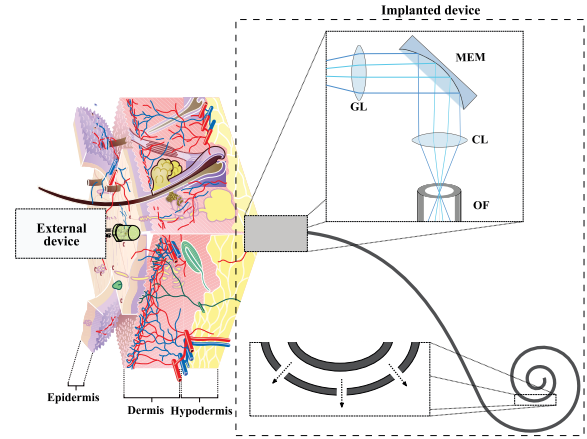


Fig. 1. The AOCI architecture.

process, but also customize its operation to the patient particularities. In the proposed architecture, the MEM is vital for the functionality of the system, since it enables the appropriate steering of the light beam toward the CL. In more detail, the MEM is able to adjust its optical properties by applying the appropriate electrical charge. The adjustment procedure can be performed once during the implantation process, while under stable operating state there is no need for any adjustment performed by the MEM and thus, since no energy is required, the MEM operates in a passive manner [27], [28].

CL: Light incident on the OF end with an angle greater than the acceptance angle will not be coupled. To prevent this, the CL is placed between the OF and the MEM to focus the signal beam in the center of the OF. Thus, the CL plays a decisive role in achieving the maximum achievable coupling efficiency. The characteristics of the CL determine the optical power that can be successfully coupled inside the OF. Note that, according to [17], the maximum achievable coupling efficiency cannot surpass 80%.

OF: Each region of the acoustic nerve is responsible for the interpretation of a specific sound frequency in the audible spectrum. Consequently, the optical stimulations must be guided toward specific photosensitive acoustic nerve regions. This task can be accomplished by utilizing the OF architecture that was proposed in [16]. The light propagates through the single-mode OF and the optical beam output from the OF behaves as a Gaussian beam [29]. It should be highlighted that, modern conventional cochlear implants house up to 22 electrodes. However, due to the low spatial resolution of the stimulation most patients perceive sound as if only 8 electrodes are functioning [30]. In that respect, it has been proven that at least 20 functional electrodes are needed for the patient to successfully perceive speech in a noisy environment [31], while this number rises to 32 in order to recognize music [32]. Since the objective of the AOCI is to achieve superior sound perception, the number of output sites must exceed 32. To satisfy the demand of emitting the optical signal inserted in the OF in different locations, based on its wavelength, we employ fiber Bragg gratings (FBGs), which are optical components with a periodic variation of the refractive index along the propagation direction in the core

of the OF [33], [34]. FBGs are low-complexity structures, have low-insertion-loss, high-wavelength-selectivity and are fully compatible with single-mode OFs. Moreover, recent technological advances enabled the construction of tilted FBGs, which filter the incident light and allow only certain wavelengths to pass through, while changing the direction of the light beam according to its tilted nature [35], [36].

III. SYSTEM MODEL

Let us assume that the optical signal, x , is emitted through a transdermal wireless channel. Thus, the received signal at the implanted device can be expressed as

$$y_1 = h_t x, \quad (1)$$

where h_t represents the optical channel coefficient [12]

$$h_t = h_l h_p. \quad (2)$$

In (2), h_l and h_p denote the deterministic channel coefficient, due to the propagation and the stochastic process that models the geometric spread, due to pointing error, respectively. The deterministic term of h_t can be expressed as

$$h_l = \exp(-(\mu_\alpha + \mu_s)\delta), \quad (3)$$

where μ_α represents the attenuation coefficient, μ_s is the scattering coefficient and δ is the total skin thickness. The skin attenuation and scattering coefficients can be derived from [37]–[43] and they depend on the wavelength of the optical beam. We highlight that the external device is in contact with the outer side of the skin, while the internal device is implanted on the bone of the skull. Thus, the distance between external and the internal device of the system can be approximated by δ . Also, it can be observed from (3) that the signal attenuation due to scattering increases with the skin thickness. However, the pointing requirement is not affected substantially due to the limited thickness of the skin, i.e., 4 – 10 mm, and the necessary directivity of the optical beam captured by the implanted device.

Next, by assuming spatial intensity of beam waist, w_δ , on the implant's plane at distance δ from the LS with divergence angle, θ , and circular aperture of radius β , the stochastic term of the channel coefficient can be approximated as

$$h_p \approx A_0 \exp\left(-\frac{2r^2}{w_{eq}^2}\right), \quad (4)$$

where

$$w_{eq}^2 = w_\delta^2 \frac{\sqrt{\pi} \operatorname{erf}(v)}{2v \exp(-v^2)}, \quad (5)$$

$$v = \frac{\sqrt{\pi}\beta}{\sqrt{2}w_\delta}, \quad (6)$$

$$w_\delta = \delta \tan\left(\frac{\theta}{2}\right), \quad (7)$$

$$A_0 = [\operatorname{erf}(v)]^2. \quad (8)$$

Notice that h_p represents the fraction of the collected power due to geometric spread with radial displacement, r , from the origin of the detector. Likewise, this is a well-known approximation that has been used in several reported contributions (see, e.g., [44], [45], and references therein).

Moreover, it is assumed that the elevation and the horizontal displacement (sway) follow independent and identical Gaussian distributions. Hence, based on [46], it can be proven that the radial displacement at the implant follows a Rayleigh distribution with a probability density function (PDF) that can be obtained as [47]

$$f_r(r) = \frac{r}{\sigma_s^2} \exp\left(-\frac{r^2}{2\sigma_s^2}\right), \quad r > 0. \quad (9)$$

The received signal, described by (1), is collected by the GL and forwarded toward the MEM. The MEM output can be expressed as

$$y_2 = G_c h_l h_p x, \quad (10)$$

where G_c denotes the collimation gain and, according to [48], can be obtained as

$$G_c = \frac{1}{\sqrt{(1-d_{in}/f)^2 + z_0^2/f^2}}, \quad (11)$$

with d_{in} being the distance between the beam waist location and the MEM surface at the point of incidence. Moreover, f is the focal length of the MEM and z_0 is the Rayleigh range of the incident beam. In addition, the beam-waist ratio has a maximum value occurring when the input distance and the focal length are equal and can be evaluated as [48]

$$G_c^* = \frac{f}{z_0}. \quad (12)$$

The optical signal reflected by the MEM is captured by the CL and forwarded inside the OF. The signal coupled into the OF can be written as

$$y_3 = \eta G_c h_l h_p x. \quad (13)$$

where η is the coupling efficiency. The following Theorem returns a novel closed-form expression for the evaluation of η .

Theorem 1: The coupling efficiency can be evaluated as

$$\eta = \left(\frac{3.83\sqrt{2}D\omega_0}{1.22\lambda F} \exp\left(-\frac{r^2}{\omega_0^2}\right) \Psi_2\left(1; 2, 1; -\frac{3.83^2 D^2 \omega_0^2}{1.22^2 \lambda^2 F^2}, \frac{r^2}{\omega_0^2}\right)\right)^2, \quad (14)$$

where ρ , D , F and ω_0 denote the radial distance on the focal plane, the focusing lens diameter, focal length and the OF mode field radius, respectively.

Proof: Please refer to Appendix A. ■

From (14), we observe that η depends on the diameter and focal length of the CL, the OF mode field radius, the transmission wavelength and the pointing errors.

The signal coupled into the OF is subject to bending and FBG losses. Thus, the optical signal that is emitted on the acoustic nerve, can be written as

$$y_4 = k\eta G_c h_l h_p x, \quad (15)$$

where k is the light beam's propagation efficiency through the OF. The bending losses of conventional OFs can be calculated using weakly guiding or adiabatic approximation [49]. However, these approximations are not valid for sharply bent microfiber, which are usually high-index-contrast waveguides. In practice, the strong optical confinement ability of the microfiber limits the power leakage (0.14 dB/90°) even for

increased bending radius or index values. Also, the losses generated by the use of FBGs are proven to be in the order of 10% [50].

The stimulation of the cochlear neurons depends on the number of photons emitted at the output of the OF [51]. When the received photons surpass a threshold, the neurons are excited and an auditory brainstem response (ABR) is triggered. In order to determine the amount of photons, we convert the optical power of the optical signal that is emitted on the cochlear neurons to the corresponding photon flux, Φ , which can be expressed as [51]

$$\Phi = \frac{\lambda}{hc} y_4, \quad (16)$$

where h and c denote the Planck's constant and the speed of light, respectively.

As indicated by the above analysis, the AOCI architecture consists of only passive components; therefore, no-noise is generated in the signal at the output of the OF. However, given the photosensitive nature of the cochlear neurons and the fact that a background fluorescence exists in the human body, a photon-shot-noise is generated [52]–[56]. In more detail, the background fluorescence that exists inside the human body is generated by unlabeled cellular elements, as well as properly and improperly targeted indicators received by the neurons. In addition, it is represented by the rate of detected photons, F_0 , in the absence of a transmission and combines fluorescence excitation, emission, and detection. The shot-noise arises from the quantum nature of light and follows a Poisson distribution, since photons arrive at the neuron continuously and independently. As a result, the additive noise follows a Poisson distribution with mean $\bar{B} = F_0\tau$, where τ is the neurons time decay constant. The probability mass function (pmf) of the photon-shot-noise can be obtained as [56]

$$p_N(n) = \frac{\bar{B}^n}{n!} e^{-\bar{B}}, \quad (17)$$

where n are the photons generated by the background fluorescence. As a result, the photon flux signal model can be written as

$$Y = \Phi + N, \quad (18)$$

where Y and N represent the photon flux received by the neurons and the background photon-shot-noise, respectively.

IV. A FEASIBILITY STUDY

In order to validate the feasibility of the AOCI and reveal the appropriate values of the design parameters, we derive the average photon flux.

Theorem 2: The average emitted photon flux can be evaluated as in (19), shown at the bottom of this page.

Proof: Please refer to Appendix B. ■

From (19) it becomes evident that the average emitted photon flux is dependent upon three terms, i.e., $(xA_0 e^{-(\mu_\alpha + \mu_s)\delta} / \lambda \sigma_s^2)$, $(D\omega_0/F)^2$ and $(2/\omega_0^2 + 2/w_{eq}^2 + 1/2\sigma_s^2)^{-1}$. The first one models the impact of the LS and the transdermal channel. We observe the average emitted photon flux increases with the transmission power, while it decreases with the wavelength, the skin thickness and the misalignment standard deviation. The second term contains the transmission wavelength and the design parameters related to the coupling of the light, i.e., OF mode field radius, CL focal length and diameter. This term is proportional to $\bar{\Phi}$ and has a more detrimental effect due to the fact that it is raised to the square. However, it should be noted that the selection of the CL and OF dimensions is bound by the geometry of the coupling phenomenon. In other words, the selection of a higher diameter CL does not ensure a higher emitted photon flux. Finally, due to the last term, $\bar{\Phi}$ increases with the OF mode field radius, the misalignment standard deviation and the equivalent beam radius.

However, after the successful excitation of a neuron, it enters a relaxation period of duration τ . This behavior can be modeled based on [56] and the received photon flux can be evaluated as

$$Y_1 = \bar{\Phi} \exp\left(-\frac{t}{\tau}\right) + F_0. \quad (20)$$

In addition, when a signal is transmitted, the average photon flux of the signal plus the background noise is their time integral, which can be expressed as

$$\bar{Y}_1 = \int_0^\tau Y_1 dt = \bar{\Phi} \frac{\tau(e-1)}{e} + \bar{B}. \quad (21)$$

Notice that (21) is the link budget of the proposed architecture and that the average received photon flux is proportional to the average emitted photon flux and the neural relaxation period. This indicates that the link budget is affected by the characteristics of the optical devices, the transdermal channel path-loss and pointing errors, as well as the background photon-shot-noise.

Although, $\bar{\Phi}$ is a widely-accepted feasibility study metric, due to the stochastic nature of the channel, it is unable to fully quantify the performance of the AOCI. Motivated by this, we defined three key-performance-indicators (KPIs), which assess the successful neural stimulation (probability of hearing), the unintentional neural stimulation (probability of false-hearing) and the neural damage (probability of neural damage). To the best of the authors knowledge, this work is one of the first that provides an engineering perspective to the important topic of CIs. As a consequence, there are no previously published papers that define these KPIs.

Definition 1: The probability of hearing can be defined as

$$P_h = P_r(Y \geq \mathcal{Y}_{th}), \quad (22)$$

$$\bar{\Phi} = \frac{kG_c h_l \lambda x A_0 \left(\frac{3.83\sqrt{2}D\omega_0}{1.22\lambda F} \right)^2}{2hc\sigma_s^2 \left(\frac{2}{\omega_0^2} + \frac{2}{w_{eq}^2} + \frac{1}{2\sigma_s^2} \right)} F^{(4)} \left[\begin{matrix} -:::-; -; -; -; -; 1; -; 1; -; 1; -; -; -; - & \frac{3.83^2 D^2 \omega_0^2}{1.22^2 \lambda^2 F^2}, \frac{3.83^2 D^2 \omega_0^2}{1.22^2 \lambda^2 F^2}, \frac{1}{\omega_0^2} \\ -:::-; -; -; -; -; -; -; -; -; -; 2; 1; 1; - & \frac{2}{\omega_0^2} + \frac{2}{w_{eq}^2} + \frac{1}{2\sigma_s^2}, \frac{2}{\omega_0^2} + \frac{2}{w_{eq}^2} + \frac{1}{2\sigma_s^2} \end{matrix} \right] \quad (19)$$

where \mathcal{Y}_{th} is the minimum required photon flux in order to achieve neural excitation.

Definition 2: The probability of false-hearing is defined as the probability to excite a neuron in the absence of transmitted signal and can be evaluated as

$$P_m = P_r(N \geq \mathcal{Y}_{th}). \quad (23)$$

The following theorem returns a closed-form expression for the probability of false-hearing.

Theorem 3: The false-hearing probability can be evaluated as

$$P_m = \frac{\Gamma(\mathcal{Y}_{th}+1, \bar{B})}{\mathcal{Y}_{th}!}. \quad (24)$$

Proof: From (23), we can rewrite the false-hearing probability as

$$P_m = \mathcal{F}_N(\mathcal{Y}_{th}), \quad (25)$$

where \mathcal{F}_N is the cumulative density function (CDF) of N . Since, N is a Poisson distributed random variable, its CDF can be obtained as

$$\mathcal{F}_N(\mathcal{Y}_{th}) = \frac{\Gamma(\mathcal{Y}_{th}+1, \bar{B})}{\mathcal{Y}_{th}!}. \quad (26)$$

From (25) and (26), we get (24). This concludes the proof. ■

Definition 3: The probability of neural damage is defined as

$$P_d = P_r(N \geq \mathcal{D}_{th} | \xi = 0) + P_r(Y \geq \mathcal{D}_{th} | \xi = 1), \quad (27)$$

where $P_r(N \geq \mathcal{D}_{th} | \xi = 0)$ and $P_r(Y \geq \mathcal{D}_{th} | \xi = 1)$ are the conditional probabilities that the instantaneous photon flux surpasses the the maximum permissible exposure (MPE) for the cochlear neurons, \mathcal{D}_{th} , in the absence and presence of optical signal, respectively. Additionally, $\xi \in \{0, 1\}$ is a binary variable that characterizes the absence ($\xi = 0$) and presence ($\xi = 1$) of optical signal.

Notice that, in practice, $N \ll \mathcal{D}_{th}$, hence, (27) can be approximated as

$$P_d \approx P_r(Y \geq \mathcal{D}_{th}). \quad (28)$$

V. NUMERICAL RESULTS AND DISCUSSION

In this section, we report numerical results, accompanied by related discussions, which highlight the feasibility and efficiency of the AOCI. In addition, insightful design guidelines for the BBs of the AOCI are extracted. Additionally, we demonstrate and compare the theoretical results with Monte Carlo simulations that verify the analytic framework. In the following figures, the dashed-line specifies the minimum photon flux required for the excitation of the cochlear neurons [7]. In addition, we point out that based on [7], the highest LS optical transmission power, 200 mW, corresponds to irradiance of approximately 12 mW/mm² on the cochlear neurons and 56 mW/mm² on the skin, which are below the respective MPE limits (~ 75 mW/mm² and 500 mW/mm²) [57], [58]. Finally, the simulation parameters are presented in Table I alongside the corresponding symbols, values and references.

In Fig. 2, the average photon flux is depicted as a function of the skin thickness and the divergence angle for optical

TABLE I
SIMULATION PARAMETERS

Parameter	Symbol	Value	References
LS divergence angle	θ	$[5 - 30]^\circ$	[13]
Wavelength	λ	594 nm	[5], [9]
Skin thickness	δ	$[4 - 10]$ mm	[15]
CL radius	D	0.1 mm	[59], [60]
OF mode field radius	ω_0	0.1 mm	[5], [7]
Time decay constant	τ	0.15 s	[56]

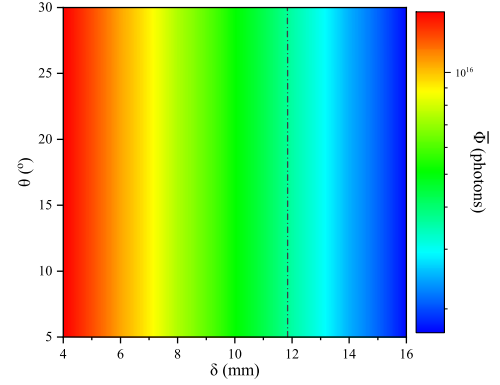


Fig. 2. Average emitted photon flux vs skin thickness and LS divergence angle, for optical transmission power of 20 mW.

transmission power of 20 mW. From this figure, it is evident that for a fixed divergence angle, the average emitted photon flux increases as the skin thickness decreases. For example, for divergence angle equal to 20°, the average emitted photon flux increases by approximately 44%, as the skin thickness decreases from 8 to 6 mm. This is expected because as the transmission distance increases, the amount of the optical power captured by the implanted device decreases. Additionally, a decrease in divergence angle, for the same skin thickness, results in an increase in the emitted photon flux. For instance, for a fixed skin thickness equal to 6 mm, as the divergence angle decreases from 30° to 20°, a 3% increase of the emitted photons is observed. This increase is anticipated because, for higher divergence angle values, the amount of light guided far from the implanted device increases. Finally, we highlight the fact that the path-loss has a more detrimental effect on the AOCI performance, compared to the non-concentration of the optical beam.

In Fig. 3, the average emitted photon flux is presented as a function of the skin thickness and optical transmission power. From this figure, it becomes obvious that, for a fixed skin thickness, as the optical transmission power of the LS decreases, the average emitted photon flux also decreases. For instance, for a skin thickness set to 6 mm, as the optical transmission power decreases from 20 to 10 mW, the average emitted photon flux decreases approximately 49%. Meanwhile, for the same optical transmission power as the skin thickness increases, the number of the emitted photons decreases. Likewise, this figure provides an illustration of the equilibrium formed between the gain from increasing optical transmission power and the possible restrictions imposed on the AOCI from the skin thickness. In other words, it indicates that for patients with increased skin thickness, the AOCI should use

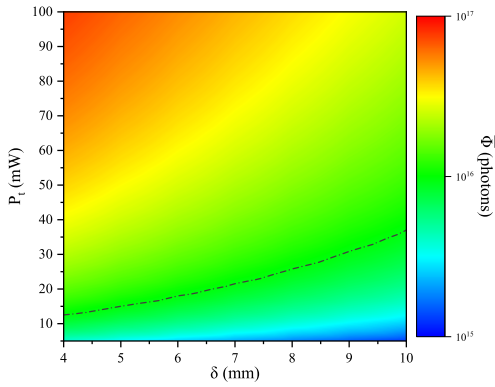


Fig. 3. Average emitted photon flux vs skin thickness and optical transmission power.

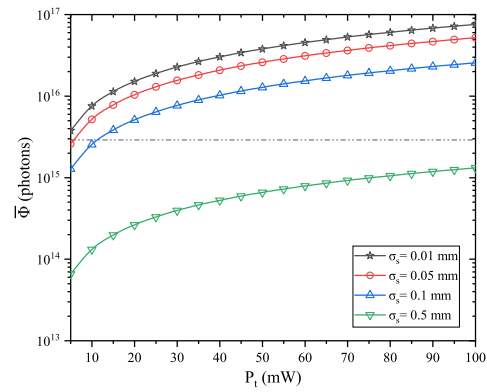


Fig. 5. Average emitted photon flux vs optical transmission power, for different values of misalignment standard deviation.

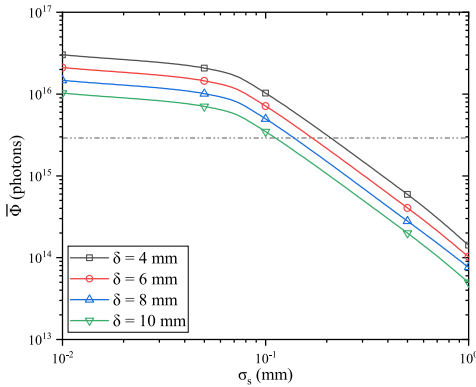


Fig. 4. Average emitted photon flux vs misalignment standard deviation, for different values of skin thickness, and optical transmission power of 40 mW.

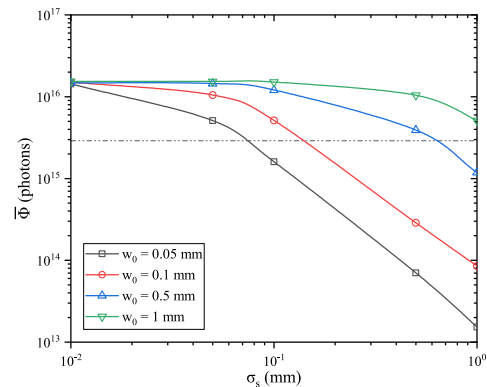


Fig. 6. Average emitted photon flux vs misalignment standard deviation, for different OF dimensions, and optical transmission power of 20 mW.

a higher power to achieve the same performance, in terms of the average emitted photon flux.

In Fig. 4, the average emitted photon flux is illustrated as a function of the misalignment standard deviation, for different values of skin thickness and optical transmission power of 40 mW. It is obvious that simulation and analytic results coincide, which verifies the validity of the theoretical framework. From this figure, we observe that for a certain standard deviation of the pointing error, as the skin thickness increases, the average emitted photon flux decreases. This is expected because the transmission distance of the optical signal increases; thus, the channel attenuation is higher. Moreover, for a fixed skin thickness, the average emitted photon flux is inversely proportional to the pointing error standard deviation. For instance, for skin thickness equal to 6 mm, as the pointing error standard deviation varies from 0.1 to 1 mm, the average emitted photon flux decreases by approximately 98%, i.e., from 7.13×10^{15} to 1.03×10^{14} photons. It is important to highlight that the misalignment between the LS and the implanted device is the determining factor.

In Fig. 5, the average emitted photon flux is illustrated as a function of the optical transmission power, for different values of the pointing errors standard deviation. As expected, for a fixed pointing error standard deviation value, an increase in the optical transmission power, results in increased number of emitted photons on the cochlear neurons. For example,

for a pointing errors standard deviation equal to 0.1 mm, as the optical transmission power increases from 10 to 20 mW, the average emitted photon flux clearly surpasses the excitation limit of the cochlear neurons. This is of high significance for the design of the AOCI because, on the one hand, the effect of the pointing errors can be mitigated by increasing P_t without surpassing the safe limits, while on the other hand, the proposed architecture is proven capable of overcoming the limitations that are entangled with the uniqueness of each human organism. Additionally, it is worth-noting that, for a fixed optical transmission power, an increase in the pointing errors standard deviation results in a decrease of the average emitted photon flux. For instance, for 20 mW optical transmission power, as the pointing errors standard deviation decreases from 0.5 to 0.1 mm, the average emitted photon flux increases by about 94%. However, for the same optical transmission power, as the pointing errors standard deviation decreases from 0.05 to 0.01 mm, the average emitted photon flux increases by 45%. This fact highlights once more the detrimental effect of the pointing errors on the performance of the AOCI and the importance to mitigate it.

A possible solution for the mitigating the impact of the pointing errors is provided by altering the characteristics of the CL and the OF, as depicted in Fig. 6. In particular, in Fig. 6, the average emitted photon flux is illustrated as a function of the pointing errors standard deviation, for different

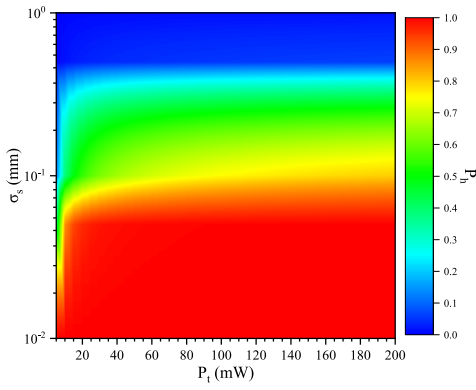


Fig. 7. Probability of hearing vs misalignment standard deviation and optical transmission power.

CL and OF dimensions, and optical transmission power of 20 mW. The validity of the theoretical framework is verified through the coincidence of the simulation and analytic results. We observe that, for a specific CL and OF pair, as the pointing errors standard deviation increases, the emitted average photon flux decreases. However, for a fixed value of pointing errors standard deviation, different characteristics of the CL and OF can achieve different average emitted photon flux performance. It is highlighted that, the selected values for CLs and OFs, which are employed in this figure, have been carefully selected in order to maintain the highest achievable coupling efficiency, i.e., approximately 80%. In more detail, as the pointing errors standard deviation increases, the impact of the characteristics of the CL and the OF on the performance of the system increases, as well. For instance, for mode field radius of 0.1 and 1 mm and the corresponding characteristics for the CL, the average emitted photon flux degrades by approximately 99% and 67%, respectively, as the pointing errors standard deviation varies from 0.1 to 1 mm. This observation reveals that it is possible to mitigate the impact of the pointing errors on the AOCI's performance by increasing the mode field radius of the OF.

In Fig. 7, the probability of hearing is depicted as a function of the pointing errors standard deviation and the optical transmission power. As expected, for a given pointing errors standard deviation, the probability of hearing increases proportionately to the optical transmission power. For example, for pointing errors standard deviation of 10^{-1} mm, as the optical transmission power varies from 20 to 120 mW, the probability of hearing increased by about 36%. In addition, for a fixed value of the optical transmission power, as the pointing errors standard deviation decreases the probability of hearing increases. For instance, for an optical transmission power of 100 mW, as the pointing errors standard deviation increases from 0.1 to 0.5 mm, the probability of hearing decreases by approximately 93%. These observations highlight the detrimental impact of the pointing errors on the systems performance, which can be mitigated by altering the optical components characteristics and increasing the optical transmission power. Finally, from this figure it becomes noticeable that for realistic values of the pointing errors standard deviation (i.e., $\sigma_s \leq 0.05$ mm), the AOCI achieves a probability of

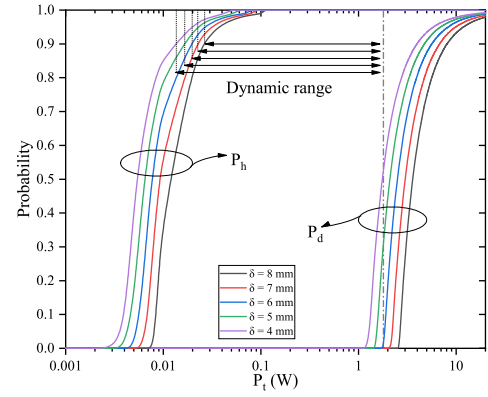


Fig. 8. Probability of hearing and probability of neural damage vs optical transmission power for different values of skin thickness, and misalignment standard deviation of 0.05 mm.

hearing higher than 90% with an optical transmission power in the order of 20 mW, while, according to (24), the probability of false-hearing is approximately zero. Note that CCIs demand a significantly additional transmission power in order to cover the needs of the implanted device, while the implanted device of the AOCI is composed only from passive elements. This indicates that the AOCI approach is a greener biomedical device paradigm in comparison with the conventional ones.

Fig. 8 presents the probability of hearing and the probability of neural damage as a function of the optical transmission power for different skin thickness values. The dashed-line specifies the MPE limit for the optical beam irradiance incident on the skin [58]. Note that, the values of the optical transmission power on the horizontal axis are presented in a logarithmic scale. We observe that for a specific skin thickness, the probability of neural damage increases with the optical transmission power, which is expected. Moreover, from this figure it becomes evident that for a specific value of optical transmission power the acoustic nerve damage probability is highly influenced by the skin thickness. For instance, for optical transmission power of 2 W and skin thickness lower than 7 mm, the damage of acoustic nerve is almost certain. It is highlighted that the values of the optical transmission power, for which the probability of neural damage is defined, i.e., higher than 1 W, are extremely high. Moreover, the MPE limit for the transdermal link is more strict than the probability of neural damage; thus, it defines the safe dynamic range of the AOCI system. In more detail, the dynamic range of the AOCI is inversely proportional to the skin thickness, i.e., as the skin thickness increases, the dynamic range decreases. For example, as skin thickness varies from 8 to 4 mm, the dynamic range increases approximately 2%. Finally, from this figure it is apparent that the proposed AOCI architecture is safe for optogenetic applications.

VI. CONCLUSION

This paper was devoted to delivering an innovative AOCI architecture and describing its BBs. Moreover, a system model that incorporates its particularities, a link budget analysis that theoretically verifies its feasibility, as well as the probabilities

of hearing, false-hearing and neural damage, which quantify its efficiency and safety for the human body, are presented. The accuracy of the theoretical analysis was verified through Monte Carlo simulations, which additionally revealed that the AOCI outperforms CCIs in terms of energy consumption, and constitutes a safe solution for a significant number of patients. Finally, both the system model and theoretical framework are expected to become the basic design tools of AOCIs.

APPENDIX A

If we assume that a Gaussian optical beam is focused on a single-mode fiber core, the coupling efficiency is given by [61, eq. (6)]

$$\eta = \frac{\left| \int_0^\infty A(\rho)M(\rho)d\rho \right|^2}{\int_0^\infty |A(\rho)|^2 d\rho}, \quad (29)$$

where, $A(\rho)$ and $M(\rho)$ can be expressed as [61, eq. (2)]

$$A(\rho) = \frac{\pi D^2}{2\lambda F} \frac{J_1\left(\frac{3.14\rho D}{\lambda F}\right)}{\left(\frac{3.14\rho D}{\lambda F}\right)}, \quad (30)$$

and

$$M(\rho) = \frac{2\sqrt{2\pi}\rho}{\omega_0} \exp\left(-\frac{\rho^2+r^2}{\omega_0^2}\right) I_0\left(\frac{2\rho r}{\omega_0^2}\right). \quad (31)$$

By substituting (30) and (31) into (29), the coupling efficiency can be rewritten as follows

$$\eta = \left| \frac{2\sqrt{2}}{\omega_0} \right|^2 \left| \int_0^\infty J_1\left(\frac{3.14\rho D}{\lambda F}\right) \exp\left(-\frac{\rho^2+r^2}{\omega_0^2}\right) I_0\left(\frac{2\rho r}{\omega_0^2}\right) d\rho \right|^2. \quad (32)$$

The coupling efficiency, from (32), can be written as follows

$$\eta = \left| \frac{2\sqrt{2}}{\omega_0} \exp\left(-\frac{r^2}{\omega_0^2}\right) \right|^2 |\mathcal{I}|^2, \quad (33)$$

where

$$\mathcal{I} = \int_0^\infty J_1\left(\frac{3.83 \times 2\rho D}{1.22\lambda F}\right) \exp\left(-\frac{\rho^2}{\omega_0^2}\right) I_0\left(\frac{2\rho r}{\omega_0^2}\right) d\rho. \quad (34)$$

By employing [62, eq. (8.441/2)] and [62, eq. (8.447/1)], (34) can be rewritten as

$$\begin{aligned} \mathcal{I} &= \int_0^\infty \sum_{m,n=0}^\infty \exp\left(-\frac{\rho^2}{\omega_0^2}\right) \\ &\times \frac{3.83\rho D (-1)^m \left(\frac{3.83 \times 2\rho D}{1.22\lambda F}\right)^{2m} \left(\frac{\rho r}{\omega_0^2}\right)^{2n}}{1.22\lambda F 4^m m!(m+1)!(n!)^2} d\rho, \end{aligned} \quad (35)$$

or equivalently

$$\mathcal{I} = \sum_{m,n=0}^\infty \frac{3.83D (-1)^m \left(\frac{3.83 \times 2D}{1.22\lambda F}\right)^{2m} \left(\frac{2r}{\omega_0^2}\right)^{2n}}{1.22\lambda F 4^{m+n} m!(m+1)!(n!)^2} \mathcal{I}_1, \quad (36)$$

with

$$\mathcal{I}_1 = \int_0^\infty \rho^{2m+2n+1} \exp\left(-\frac{\rho^2}{\omega_0^2}\right) d\rho. \quad (37)$$

Furthermore, by employing [62, eq. (2.33/10)], (37) can be expressed as

$$\mathcal{I}_1 = \frac{\Gamma(m+n+1)}{2(\omega_0^2)^{m+n+1}}. \quad (38)$$

Next, by substituting (38) into (36), the former can be equivalently written as

$$\mathcal{I} = \frac{3.83D\omega_0^2}{1.22 \times 2\lambda F} \sum_{m,n=0}^\infty \frac{(-1)^m \left(\frac{3.83 \times 2D}{1.22\lambda F}\right)^{2m} \left(\frac{2r}{\omega_0^2}\right)^{2n} \Gamma(m+n+1)}{(4\omega_0^2)^{m+n} m!(m+1)!(n!)^2}. \quad (39)$$

Moreover, by taking into account that $\Gamma(m+n+1) = \Gamma(1)(1)_{m+n}$, $(m+1)! = \Gamma(m+2) = (2)_m$, $\Gamma(1) = 1$, and $(n!)^2 = \Gamma(1)(1)_n$, (39) can be expressed as

$$\mathcal{I} = \frac{3.83D\omega_0^2}{1.22 \times 2\lambda F} \sum_{m,n=0}^\infty \frac{(1)_{m+n} \left(\frac{3.83^2 D^2 \omega_0^2}{1.22^2 \lambda^2 F^2}\right)^m \left(\frac{r^2}{\omega_0^2}\right)^n}{(1)_n (2)_m m! n!}. \quad (40)$$

Notice that (40) is the fifth Humbert hypergeometric series [21, eq. (7.2.4/10)]. Hence, (40) can be expressed as follows

$$\mathcal{I} = \frac{3.83D\omega_0^2}{1.22 \times 2\lambda F} \Psi_2\left(1; 2, 1; -\frac{3.83^2 D^2 \omega_0^2}{1.22^2 \lambda^2 F^2}, \frac{r^2}{\omega_0^2}\right). \quad (41)$$

Finally, by substituting (41) into (33), the coupling efficiency can be equivalently rewritten as in (14). This concludes the proof.

APPENDIX B

The expected value of the photon flux with respect to the misalignment fading can be evaluated as

$$\bar{\Phi} = \int_0^\infty \Phi(r) f_r(r) dr, \quad (42)$$

or equivalently,

$$\bar{\Phi} = \int_0^\infty k\eta(r) G_c h_l h_p(r) \frac{\lambda}{hc} x \frac{r}{\sigma_s^2} \exp\left(-\frac{r^2}{2\sigma_s^2}\right) dr, \quad (43)$$

where, only η and h_p are affected by the pointing error, r . By substituting (14) and (4) into (43), the average emitted photon flux can be rewritten as

$$\begin{aligned} \bar{\Phi} &= k G_c h_l \frac{\lambda}{hc} x A_0 \frac{1}{\sigma_s^2} \left(\frac{3.83\sqrt{2}D\omega_0}{1.22\lambda F}\right)^2 \\ &\times \int_0^\infty r \exp\left(-\frac{2r^2}{\omega_0^2} - \frac{2r^2}{\omega_q^2} - \frac{r^2}{2\sigma_s^2}\right) K(r) dr, \end{aligned} \quad (44)$$

where

$$K(r) = \left(\sum_{m=0}^\infty C_m\right)^2, \quad (45)$$

$$C_m = \sum_{n=0}^\infty \frac{(1)_{m+n} \left(-\frac{3.83^2 D^2 \omega_0^2}{1.22^2 \lambda^2 F^2}\right)^m \left(\frac{r^2}{\omega_0^2}\right)^n}{(1)_n (2)_m m! n!}. \quad (46)$$

Moreover, (45) can be equivalently written as

$$K(r) = \sum_{m,k=0}^\infty C_m C_k. \quad (47)$$

By using (46), (47) can be expressed as

$$K(r) = \sum_{m,k,n,l=0}^\infty \frac{(1)_{m+n}(1)_{k+l} \left(-\frac{3.83^2 D^2 \omega_0^2}{1.22^2 \lambda^2 F^2}\right)^{m+k} \left(\frac{r^2}{\omega_0^2}\right)^{n+l}}{(1)_n (2)_m (1)_l (2)_k m! n! k! l!}. \quad (48)$$

$$\Lambda(r) = \frac{1}{2} \left(\frac{2}{\omega_0^2} + \frac{2}{w_{eq}^2} + \frac{1}{2\sigma_s^2} \right)^{-1} \sum_{m,k,n,l=0}^{\infty} \frac{{}^{(1)}_{m+n} {}^{(1)}_{k+l} {}^{(1)}_{n+l} \left(-\frac{3.83^2 D^2 \omega_0^2}{1.22^2 \lambda^2 F^2} \right)^{m+k} \left(\frac{\frac{1}{\omega_0^2}}{\frac{2}{\omega_0^2} + \frac{2}{w_{eq}^2} + \frac{1}{2\sigma_s^2}} \right)^{n+l}}{({}^{(1)}_n {}^{(2)}_m {}^{(1)}_l {}^{(2)}_k m! n! k! l!)} \quad (51)$$

$$\Lambda(r) = \frac{1}{2} \left(\frac{2}{\omega_0^2} + \frac{2}{w_{eq}^2} + \frac{1}{2\sigma_s^2} \right)^{-1} F^{(4)} \left[\begin{matrix} -:-:-; -; -; -:-; 1; -; 1; -; 1:-; -; -; -; 3.83^2 D^2 \omega_0^2, & 3.83^2 D^2 \omega_0^2, & \frac{1}{\omega_0^2} \\ -:-:-; -; -; -:-; -; -; -:-; -2; 2; 1; 1, & -1.22^2 \lambda^2 F^2, & -1.22^2 \lambda^2 F^2, & \frac{2}{\omega_0^2} + \frac{2}{w_{eq}^2} + \frac{1}{2\sigma_s^2}, & \frac{2}{\omega_0^2} + \frac{2}{w_{eq}^2} + \frac{1}{2\sigma_s^2} \end{matrix} \right] \quad (52)$$

Next, by using (48), (19) can be rewritten as

$$\bar{\Phi} = kG_c h_l \frac{\lambda}{hc} x A_0 \frac{1}{\sigma_s^2} \left(\frac{3.83\sqrt{2}D\omega_0}{1.22\lambda F} \right)^2 \Lambda(r), \quad (49)$$

where

$$\Lambda(r) = \sum_{m,k,n,l=0}^{\infty} \frac{{}^{(1)}_{m+n} {}^{(1)}_{k+l} \left(-\frac{3.83^2 D^2 \omega_0^2}{1.22^2 \lambda^2 F^2} \right)^{m+k} \left(\frac{1}{\omega_0^2} \right)^{n+l}}{({}^{(1)}_n {}^{(2)}_m {}^{(1)}_l {}^{(2)}_k m! n! k! l!)} \times \int_0^{\infty} \exp\left(-\frac{2r^2}{\omega_0^2} - \frac{2r^2}{w_{eq}^2} - \frac{r^2}{2\sigma_s^2}\right) r^{2(n+l)+1} dr. \quad (50)$$

After performing the integration (50), can be equivalently written as in (51), shown at the top of this page. Notice that, according to [22, eq. (16)], (51) can be expressed in terms of the general quadruple hypergeometric function as in (52), given at the top of the page. Finally, by substituting (52) into (49), the average emitted photon flux can be written as in (19). This concludes the proof.

REFERENCES

- [1] T. Dombrowski, V. Rankovic, and T. Moser, "Toward the optical cochlear implant," *Cold Spring Harbor Perspect. Med.*, vol. 1, no. 9, Oct. 2018, Art. no. a033225.
- [2] B. S. Wilson and M. F. Dorman, "Cochlear implants: A remarkable past and a brilliant future," *Hearing Res.*, vol. 242, nos. 1–2, pp. 3–21, Aug. 2008.
- [3] F. G. Zeng, S. Rebscher, W. Harrison, X. Sun, and H. Feng, "Cochlear implants: System design, integration, and evaluation," *IEEE Rev. Biomed. Eng.*, vol. 1, no. 1, pp. 115–142, Nov. 2008.
- [4] B. S. Wilson, "The modern cochlear implant: A triumph of biomedical engineering and the first substantial restoration of human sense using a medical intervention," *IEEE Pulse*, vol. 8, no. 2, pp. 29–32, Mar. 2017.
- [5] T. Moser and A. Dieter, "Towards optogenetic approaches for hearing restoration," *Biochem. Biophys. Res. Commun.*, vol. 527, no. 2, pp. 337–342, Feb. 2020.
- [6] V. H. Hernandez *et al.*, "Optogenetic stimulation of the auditory pathway," *J. Clin. Invest.*, vol. 124, no. 3, pp. 1114–1129, Feb. 2014.
- [7] C. Wrobel *et al.*, "Optogenetic stimulation of cochlear neurons activates the auditory pathway and restores auditory-driven behavior in deaf adult gerbils," *Sci. Transl. Med.*, vol. 10, no. 449, Jul. 2018, Art. no. eaao540.
- [8] T. Mager *et al.*, "High frequency neural spiking and auditory signaling by ultrafast RED-shifted optogenetics," *Nat. Commun.*, vol. 9, no. 1, p. 1750, May 2018.
- [9] D. Keppeler *et al.*, "Ultrafast optogenetic stimulation of the auditory pathway by targeting-optimized chronos," *EMBO J.*, vol. 37, no. 24, Nov. 2018, Art. no. e99649.
- [10] Y. Xu *et al.*, "Multichannel optodes for photonic stimulation," *Neurophotonics*, vol. 5, no. 4, p. 1, Oct. 2018.
- [11] W. L. Hart, T. Kameneva, A. K. Wise, and P. R. Stoddart, "Biological considerations of optical interfaces for neuromodulation," *Adv. Opt. Mater.*, vol. 7, no. 19, Jul. 2019, Art. no. 1900385.
- [12] S. E. Trevlakis, A.-A. A. Boulogeorgos, P. C. Sofotasios, S. Muhaidat, and G. K. Karagiannidis, "Optical wireless cochlear implants," *Biomed. Opt. Exp.*, vol. 10, no. 2, pp. 707–730, Nov. 2019.
- [13] D. M. Ackermann, Jr., B. Smith, X.-F. Wang, K. L. Kilgore, and P. H. Peckham, "Designing the optical interface of a transcutaneous optical telemetry link," *IEEE Trans. Biomed. Eng.*, vol. 55, no. 4, pp. 1365–1373, Apr. 2008.
- [14] Y. Gil, N. Rotter, and S. Arnon, "Feasibility of retroreflective transdermal optical wireless communication," *Appl. Opt.*, vol. 51, no. 18, pp. 4232–4239, Jun. 2012.
- [15] T. Liu, J. Anders, and M. Ortmanns, "Bidirectional optical transcutaneous telemetric link for brain machine interface," *Electron. Lett.*, vol. 51, no. 24, pp. 1969–1971, Nov. 2015.
- [16] J. D. Wells *et al.*, "Laser-based nerve stimulators for, e.g., hearing restoration in cochlear prostheses and method," U.S. Patent 8792978, Jul. 29, 2014.
- [17] H. Nguyen *et al.*, "Fabrication of multipoint side-firing optical fiber by laser micro-ablation," *Opt. Lett.*, vol. 42, no. 9, pp. 1808–1811, Apr. 2017.
- [18] F. Pisanello *et al.*, "Multipoint-emitting optical fibers for spatially addressable *in vivo* optogenetics," *Neuron*, vol. 82, no. 6, pp. 1245–1254, Jun. 2014.
- [19] M. Pisanello *et al.*, "Tailoring light delivery for optogenetics by modal demultiplexing in tapered optical fibers," *Sci. Rep.*, vol. 8, no. 1, p. 4467, Oct. 2018.
- [20] F. Pisano *et al.*, "Focused ion beam nanomachining of tapered optical fibers for patterned light delivery," *Microelectron. Eng.*, vol. 195, pp. 41–49, Mar. 2018.
- [21] A. P. Prudnikov, Y. A. Bryčkov, and O. I. Maričev, *Integrals and Series of Special Functions*. Moscow, Russia: Science, 1983.
- [22] M. Saigo, "On properties of hypergeometric functions of three variables, F_M and F_G ," *Rendiconti del Circolo Matematico di Palermo*, vol. 37, no. 3, pp. 449–468, Sep. 1988.
- [23] P. Oltulu, B. Ince, N. Kokbudak, S. Findik, and F. Kilinc, "Measurement of epidermis, dermis, and total skin thicknesses from six different body regions with a new ethical histometric technique," *Turkish J. Plastic Surg.*, vol. 26, no. 2, p. 56, 2018.
- [24] Y. Zou, W. Zhang, F. Tian, F. S. Chau, and G. Zhou, "Development of miniature tunable multi-element Alvarez lenses," *IEEE J. Sel. Top. Quantum Electron.*, vol. 21, no. 4, pp. 100–107, Jul. 2015.
- [25] K. Hwang, Y.-H. Seo, and K.-H. Jeong, "Microscanners for optical endomicroscopic applications," *Micro Nano Syst. Lett.*, vol. 5, no. 1, p. 1, Jan. 2017.
- [26] G. Zhou and C. Lee, Eds., *Optical MEMS, Nanophotonics, and Their Applications*. Hoboken, NJ, USA: CRC Press, Dec. 2017.
- [27] F. Khoshnoud and C. W. de Silva, "Recent advances in MEMS sensor technology—biomedical applications," *IEEE Instrum. Meas. Mag.*, vol. 15, no. 1, pp. 8–14, Feb. 2012.
- [28] A. S. Sezen, S. Sivaramakrishnan, S. Hur, R. Rajamani, W. Robbins, and B. J. Nelson, "Passive wireless MEMS microphones for biomedical applications," *J. Biomech. Eng.*, vol. 127, no. 6, pp. 1030–1034, Jul. 2005.
- [29] D. Marcuse, "Gaussian approximation of the fundamental modes of graded-index fibers," *J. Opt. Soc. Amer.*, vol. 68, no. 1, p. 103, Jan. 1978.
- [30] A. G. Srinivasan, D. M. Landsberger, and R. V. Shannon, "Current focusing sharpens local peaks of excitation in cochlear implant stimulation," *Hearing Res.*, vol. 270, nos. 1–2, pp. 89–100, Dec. 2010.
- [31] L. M. Friesen, R. V. Shannon, D. Baskent, and X. Wang, "Speech recognition in noise as a function of the number of spectral channels: Comparison of acoustic hearing and cochlear implants," *J. Acoust. Soc. America*, vol. 110, no. 2, pp. 1150–1163, Aug. 2001.

- [32] Y.-Y. Kong, R. Cruz, J. A. Jones, and F.-G. Zeng, "Music perception with temporal cues in acoustic and electric hearing," *Ear Hearing*, vol. 25, no. 2, pp. 173–185, Apr. 2004.
- [33] K. Zhou, L. Zhang, X. Chen, and I. Bennion, "Optic sensors of high refractive-index responsivity and low thermal cross sensitivity that use fiber Bragg gratings of $> 80^\circ$ tilted structures," *Opt. Lett.*, vol. 31, no. 9, pp. 1193–1195, May 2006.
- [34] R. Cotillard, G. Laffont, and P. Ferdinand, "Regeneration of tilted fiber Bragg gratings," in *Proc. 23rd Int. Conf. Opt. Fibre Sensors*, Jun. 2014, Art. no. 91572S.
- [35] G. Bharathan, D. D. Hudson, R. I. Woodward, S. D. Jackson, and A. Fuerbach, "In-fiber polarizer based on a 45-degree tilted fluoride fiber BRAGG grating for mid-infrared fiber laser technology," *OSA Continuum*, vol. 1, no. 1, pp. 56–63, Sep. 2018.
- [36] C. Mou, K. Zhou, L. Zhang, and I. Bennion, "Characterization of 45° -tilted fiber grating and its polarization function in fiber ring laser," *J. Opt. Soc. Amer. B*, vol. 26, no. 10, p. 1905, Sep. 2009.
- [37] S. Trevlakis, A.-A. Boulogeorgos, and G. Karagiannidis, "Signal quality assessment for transdermal optical wireless communications under pointing errors," *Technologies*, vol. 6, no. 4, p. 109, 2018.
- [38] T. Lister, P. A. Wright, and P. H. Chappell, "Optical properties of human skin," *J. Biomed. Opt.*, vol. 17, no. 9, Sep 2012, Art. no. 0909011.
- [39] N. Bosschaart, R. Mentink, J. H. Kok, T. G. van Leeuwen, and M. C. G. Aalders, "Optical properties of neonatal skin measured *in vivo* as a function of age and skin pigmentation," *J. Biomed. Opt.*, vol. 16, no. 9, 2011, Art. no. 097003.
- [40] A. N. Bashkatov, E. A. Genina, and V. V. Tuchin, "Optical properties of skin, subcutaneous, and muscle tissues: A review," *J. Innov. Opt. Health Sci.*, vol. 4, no. 1, pp. 9–38, Jan. 2011.
- [41] A. Bashkatov, E. Genina, V. Kochubey, and V. Tuchin, "Optical properties of human skin, subcutaneous and mucous tissues in the wavelength range from 400 to 2000 nm," *J. Phys. D Appl. Phys.*, vol. 38, no. 15, p. 2543, Jul. 2005.
- [42] E. K. Chan, B. Sorg, D. Protsenko, M. O'Neil, M. Motamedi, and A. J. Welch, "Effects of compression on soft tissue optical properties," *IEEE J. Sel. Topics Quantum Electron.*, vol. 2, no. 4, pp. 943–950, Dec. 1996.
- [43] M. Van Gemert, S. L. Jacques, H. Sterenborg, and W. Star, "Skin optics," *IEEE Trans. Biomed. Eng.*, vol. 36, no. 12, pp. 1146–1154, Dec. 1989.
- [44] A. A. Farid and S. Hranilovic, "Outage capacity optimization for free-space optical links with pointing errors," *J. Lightw. Technol.*, vol. 25, no. 7, pp. 1702–1710, Jul. 2007.
- [45] H. G. Sandalidis, T. A. Tsiftsis, G. K. Karagiannidis, and M. Uysal, "BER performance of FSO links over strong atmospheric turbulence channels with pointing errors," *IEEE Commun. Lett.*, vol. 12, no. 1, pp. 44–46, Jan. 2008.
- [46] S. Arnon, "Effects of atmospheric turbulence and building sway on optical wireless-communication systems," *Opt. Lett.*, vol. 28, no. 2, pp. 129–131, Jan. 2003.
- [47] A. Papoulis and S. Pillai, *Probability, Random Variables, and Stochastic Processes* (McGraw-Hill Series in Electrical Engineering: Communications and Signal Processing). Boston, MA, USA: Tata McGraw-Hill, Jan. 2002.
- [48] Y. Sabry, D. Khalil, B. Saadany, and T. Bourouina, "In-plane optical beam collimation using a three-dimensional curved MEMS mirror," *Micromachines*, vol. 8, no. 5, p. 134, Apr. 2017.
- [49] H. Yu *et al.*, "Modeling bending losses of optical nanofibers or nanowires," *Appl. Opt.*, vol. 48, no. 22, pp. 4365–4369, Jul. 2009.
- [50] G. Wang, C. Wang, Z. Yan, and L. Zhang, "Highly efficient spectrally encoded imaging using a 45° tilted fiber grating," *Opt. Lett.*, vol. 41, no. 11, p. 2398, May 2016.
- [51] R. H. Hadfield, "Single-photon detectors for optical quantum information applications," *Nat. Photon.*, vol. 3, no. 12, pp. 696–705, Dec. 2009.
- [52] L. Sjulson and G. Miesenböck, "Optical recording of action potentials and other discrete physiological events: A perspective from signal detection theory," *Physiology*, vol. 22, no. 1, pp. 47–55, Feb. 2007.
- [53] T. Hendel, M. Mank, B. Schnell, O. Griesbeck, A. Borst, and D. F. Reiff, "Fluorescence changes of genetic calcium indicators and OGB-1 correlated with neural activity and calcium *in vivo* and *in vitro*," *J. Neurosci.*, vol. 28, no. 29, pp. 7399–7411, Jul. 2008.
- [54] T. Sasaki, N. Takahashi, N. Matsuki, and Y. Ikegaya, "Fast and accurate detection of action potentials from somatic calcium fluctuations," *J. Neurophysiol.*, vol. 100, no. 3, pp. 1668–1676, Sep. 2008.
- [55] J. T. Vogelstein, B. O. Watson, A. M. Packer, R. Yuste, B. Jedynak, and L. Paninski, "Spike inference from calcium imaging using sequential Monte Carlo methods," *Biophys. J.*, vol. 97, no. 2, pp. 636–655, Jul. 2009.
- [56] B. A. Wilt, J. E. Fitzgerald, and M. J. Schnitzer, "Photon shot noise limits on optical detection of neuronal spikes and estimation of spike timing," *Biophys. J.*, vol. 104, no. 1, pp. 51–62, Jan. 2013.
- [57] X. Han, "In vivo application of optogenetics for neural circuit analysis," *ACS Chem. Neurosci.*, vol. 3, no. 8, pp. 577–584, Jul. 2012.
- [58] International Commission on Non-Ionizing Radiation Protection, "ICNIRP guidelines on limits of exposure to laser radiation of wavelengths between 180 nm and 1,000 μm ," *Health Phys.*, vol. 105, no. 3, pp. 271–295, Sep. 2013.
- [59] J. Jahns, Q. Cao, and S. Sinzinger, "Micro- and nanooptics—An overview," *Laser Photon. Rev.*, vol. 2, no. 4, pp. 249–263, Aug. 2008.
- [60] H.-M. Yang, S.-Y. Huang, C.-W. Lee, T.-S. Lay, and W.-H. Cheng, "High-coupling tapered hyperbolic fiber microlens and taper asymmetry effect," *J. Lightw. Technol.*, vol. 22, no. 5, pp. 1395–1401, May 2004.
- [61] M. Toyoshima, "Maximum fiber coupling efficiency and optimum beam size in the presence of random angular jitter for free-space laser systems and their applications," *J. Opt. Soc. Amer. A*, vol. 23, no. 9, p. 2246, Sep. 2006.
- [62] I. S. Gradshteyn and I. M. Ryzhik, *Table of Integrals, Series, and Products*, 7th ed. Amsterdam, The Netherlands: Elsevier, 2007.



Stylianos E. Trevlakis (Student Member, IEEE) was born in Thessaloniki, Greece, in 1991. He received the Diploma degree (five years) in electrical and computer engineering from the Aristotle University of Thessaloniki in 2016, where he is currently pursuing the Ph.D. degree with WCSG under the leadership of Prof. Karagiannidis.

He served in the Hellenic Army for nine months in the Research Office as well as with the Office of Research and Informatics, School of Management and Officers. In 2017, he joined the Information Technologies Institute. His research interests are in the area of wireless communications, with emphasis on optical wireless communications, and communications and signal processing for biomedical engineering.



Alexandros-Apostolos A. Boulogeorgos (Senior Member, IEEE) was born in Trikala, Greece, in 1988. He received the Diploma degree (five years) in electrical and computer engineering (ECE) and the Ph.D. degree in wireless communications from the Aristotle University of Thessaloniki (AUTH) in 2012 and 2016, respectively.

He has been a member of the Wireless Communications System Group, AUTH, since November 2012. In 2017, he joined the Information Technologies Institute and in November 2017, he joined the Department of Digital Systems, University of Piraeus. From October 2012 until September 2016, he was a Teaching Assistant with the Department of ECE, AUTH, whereas since February 2017, he has been serving as an Adjunct Lecturer with the Department of ECE, University of Western Macedonia and as a Visiting Lecturer with the Department of Computer Science and Biomedical Informatics, University of Thessaly. His current research interests span in the area of wireless communications and networks with emphasis in high-frequency communications, optical wireless communications, and communications for biomedical applications.

Dr. Boulogeorgos was awarded the Distinction Scholarship Award of the Research Committee of AUTH in 2014, was recognized as an Exemplary Reviewer by IEEE COMMUNICATION LETTERS in 2016 (top 3% of reviewers) and was named a Top Peer Reviewer (<1%) in Cross-Field and Computer Science in the Global Peer Review Awards 2019, which was presented by the Web of Science and Publons. He has been a member of the technical program committees of several IEEE and non-IEEE conferences and served as a reviewer in various IEEE journals and conferences.



Nestor D. Chatzidiamantis (Member, IEEE) was born in Los Angeles, CA, USA, in 1981. He received the Diploma degree (five years) in electrical and computer engineering (ECE) from the Aristotle University of Thessaloniki, Greece, in 2005, the M.Sc. degree in telecommunication networks and software from the University of Surrey, U.K., in 2006, and the Ph.D. degree from the ECE Department, AUTH, in 2012.

From 2012 to 2015, he was a Postdoctoral Research Associate with AUTH, and from 2016 to 2018, a Senior Engineer with the Hellenic Electricity Distribution Network Operator. Since 2018, he has been an Assistant Professor with the ECE Department, AUTH and a member of the Telecommunications Laboratory. His research areas span signal processing techniques for communication systems, performance analysis of wireless communication systems over fading channels, communications theory, cognitive radio, and free-space optical communications.



George K. Karagiannidis (Fellow, IEEE) was born in Pithagorion, Greece. He received the University Diploma (five years) and Ph.D. degrees in electrical and computer engineering from the University of Patras in 1987 and 1999, respectively.

From 2000 to 2004, he was a Senior Researcher with the Institute for Space Applications and Remote Sensing, National Observatory of Athens, Greece. In June 2004, he joined the faculty of the Aristotle University of Thessaloniki, Greece, where he is currently a Professor with the Electrical and Computer Engineering Department and the Head of the Wireless Communications Systems Group. He is also an Honorary Professor with South West Jiaotong University, Chengdu, China. His research interests are in the broad area of digital communications systems and signal processing, with emphasis on wireless communications, optical wireless communications, wireless power transfer and applications, and communications and signal processing for biomedical engineering.

Dr. Karagiannidis has been involved as a general chair, the technical program chair, and a member of the technical program committees in several IEEE and non-IEEE conferences. He was an Editor for several IEEE journals, and from 2012 to 2015, he was the Editor-in-Chief of IEEE COMMUNICATIONS LETTERS. He currently serves as an Associate Editor-in-Chief for the IEEE OPEN JOURNAL OF COMMUNICATIONS SOCIETY. He is one of the highly cited authors across all areas of electrical engineering, recognized by Clarivate Analytics as a Web of Science Highly Cited Researcher in the five consecutive years from 2015 to 2019.